Turkish Journal of Physics

http://journals.tubitak.gov.tr/physics/

Research Article

Turk J Phys
(2014) 38: 450 – 462

doi:10.3906/fiz-1405-4

Optical and magnetic properties of (Er, F) co-doped SnO_2 nanocrystals

Vinod KUMAR, Sitharaman UMA, Rajamani NAGARAJAN*
Materials Chemistry Group, Department of Chemistry, University of Delhi, Delhi, India

Received: 08.05.2014 • **Accepted:** 15.07.2014 • **Published Online:** 10.11.2014 • **Printed:** 28.11.2014

Abstract: Uniformly (Er, F) co-doped SnO_2 nanocrystals, obtained by a low-temperature solution-based method, were characterized by a variety of analytical techniques. The structure, morphology, and ratio of the elements were confirmed by PXRD, SEM, and TEM analysis, respectively. From XPS analysis, atomic concentrations of Sn, O, and F were quantified. Interparticle pore size increased significantly (with a mean pore diameter of 25.82 nm) in the co-doped sample. Higher in-plane oxygen vacancies and bands due to multiphonon scattering were observed in the Raman spectrum of the sample. The defect traps in the sample were experimentally determined using TL spectroscopy. A broad intense glow curve at 485 K and a weak emission at 600 K in the TL spectrum were quenched on exposure to UV radiation. A large blue shift of the exciton absorption (due to the Moss–Burstein effect) and sharp bands due to intraconfigurational $f - f$ transitions were observed for (Er, F) co-doped SnO_2 with an estimated band gap of 4.18 eV. From the photoluminescence spectral studies, 3 types of emission centers at 471 nm, 546 nm, and 627 nm were detected. Co-doping stabilized ferromagnetism in SnO_2 at room temperature.

Key words: Luminescence, ferromagnetism, defects, Moss–Burstein effect, nanocrystalline

1. Introduction

Various chemical strategies such as cation doping, anion doping, cation–cation co-doping, cation–anion co-doping, and anion–anion co-doping are being adopted to engineer the band gap of wide band gap oxide semiconductors, ZnO, TiO_2, CeO_2 and SnO_2 [1–5]. Among these, the cation–anion co-doping strategy is the least investigated and is gaining momentum for the following reasons: 1) it introduces charge compensation between dopants, thereby reducing the number of recombination centers and promoting the electron–hole pair separation to stimulate the change in the band gap by eliminating the impurity states; 2) it can facilitate the overall mixing of the impurity states and VB/CB by adjusting the position of the band gap to obtain an optimized narrow value; 3) it can effectively reduce the formation energy of the combination defects as compared to singly doped systems. Among the co-dopants, doping with 2 cations has been pursued due to the easy experimental conditions for their fabrication [6,7]. Anion–anion co-doping of these oxides is increasingly becoming viable by solution-based synthetic methods [8,9]. The cation–anion co-doping approach produces changes in the conduction and valence bands of these semiconductors simultaneously and can manifest in many interesting optoelectronic properties arising from the defect chemistry and physics, leading to expansion of functions.

SnO_2, an n-type wide band gap semiconductor, enjoys a unique status for exhibiting multifunctions for a variety of reasons such as larger exciton binding energy and high chemical and mechanical stabilities

*Correspondence: rnagarajan@chemistry.du.ac.in

with unique photoelectronic properties [1,10]. The multifunctional character of SnO_2 basically emerges from the flexible nature of the structure, having cations with mixed valence states and anions with deficiencies (vacancies). The greater contributions of lattice vibrations in imparting applications to SnO_2 for its use as solid-state gas sensor material, oxidation catalyst, and transparent conductor have been excellently reviewed in the literature [11]. As compared to single cation or anion doping in SnO_2, studies on cation–anion co-doped systems are few. Nb/F co-doped SnO_2 thin films were fabricated by spray pyrolysis procedure by Turgut et al. [12] with the primary objective of tuning the optoelectronic properties, in which the niobium content was varied between 0 and 4 at.% with fixed fluoride content of 10 wt.%. Huang et al. [13] synthesized gallium and nitrogen co-doped tin oxide (SnO_2: Ga/N) films at 500 °C using the MOCVD method to tune the band gap and the conductivity. Moharrami et al. [14] investigated the co-doping of S and Al in SnO_2 films deposited by spray pyrolysis technique. The optical band gap values were found to be in the range of 3.8–4.2 eV. Majority charge carriers were found to change from electrons to holes for S-doping in SnO_2: Al (40 at.%) thin films. On increasing sulfide concentration, impurity phases such as S, SnS, SnS_2, and Sn_2S_3 were observed along with cassiterite SnO_2. The best photoconductive property was realized for SnO_2 thin films co-doped with 40 at.% Al and 5 at.% S. Fe-N co-doped SnO_2 powders were synthesized by chemical coprecipitation method and their magnetization studies were reported [15]. The hole (defect) generated by the nitrogen doping at the oxygen site induced ferromagnetism in the SnO_2 samples, quite the opposite of the singly Fe-doped SnO_2 exhibiting a paramagnetic character.

Rare earth ions having rich spectroscopic properties have been the prime choice for cations so as to append spectroscopic functions to SnO_2. Furthermore, Er-doped SnO_2 structures have been reported as potential candidates as waveguides, electroluminescent displays, or building blocks for advanced materials [16]. While numerous reports are available on the F-doping of SnO_2 (both in films and in powders) [17,18], limited studies exist on Er-doping in SnO_2 because of the enormous size difference between Er^{3+} and Sn^{4+} and the preference of Er^{3+} to have coordination numbers greater than 6 [16,19–21]. The present paper describes the synthesis of SnO_2 nanocrystals co-doped with Er^{3+} and F^- using a single-source precursor. The obtained nanocrystals were characterized by powder X-ray diffraction (PXRD) patterns and SEM, TEM, XPS, UV-visible diffuse reflectance spectroscopic, Raman spectroscopic, and photoluminescence (PL) spectroscopic techniques. Surface area and pore size analyses of the co-doped SnO_2 samples were performed. Various trapped states were analyzed by thermoluminescence (TL), a powerful spectroscopy technique that determines the localized states as well as the recombination centers leading to radiative transition simultaneously. As the co-doping approach has been found to induce ferromagnetic ordering in wide band gap semiconductors such as ZnO, TiO_2, and SnO_2 [22,23], the magnetic interactions between the hole and the electrons in the (Er, F) co-doped SnO_2 system was also studied.

2. Experimental

2.1. Synthesis

Er and F co-doped SnO_2 nanocrystals were prepared using a single-source precursor approach [17]. First, 1 mol% Er-doped $KSnF_3$ was synthesized from $SnCl_2.2H_2O$ (99.9%, Sigma Aldrich), KF (99%, AR grade, CDH), and $ErCl_3.6H_2O$ (99.9%, Sigma Aldrich). Typically, 1.128 g of $SnCl_2.2H_2O$, 0.0065 g of $ErCl_3.6H_2O$, and 0.8715 g of KF were mixed in methanol and kept for 2 h under constant stirring. A white-colored suspension appeared and it was separated by centrifugation and washed several times with distilled water. Next, 0.25 g of

1 mol% Er-doped $KSnF_3$ was refluxed with a mixture containing 30 mL of 30% H_2O_2 and 70 mL of methanol (CH_3OH) for 10 h at 100 °C. A white-colored suspension was obtained, was separated by centrifugation, and was dried naturally over a desiccant.

2.2. Characterization

PXRD patterns were recorded using a high-resolution PANanalytical diffractometer, equipped with PIXcel^{3D} detector employing CuK_α radiation (λ = 1.5418 Å) with a scan rate of 1.0 s/step and a step size of 0.02° at 298 K over the range of 2θ = 15°–70°. Diffuse reflectance spectra of the samples were obtained using a PerkinElmer UV-Vis spectrophotometer Lambda-35 with $BaSO_4$ as the reference. Thermogravimetric analysis was carried out using a PerkinElmer Pyris Diamond in nitrogen atmosphere at the heating rate of 5 °C/min from 25 to 900 °C. FT-IR spectra were collected using a PerkinElmer 2000 spectrometer using KBr disks. Raman spectra were recorded using a Renishaw via a microscope system with an Ar^+ laser (λ = 514.5 nm). The Brunauer–Emmett–Teller (BET) surface area of the samples was obtained from physical adsorption of N_2 at 77 K using a Belsorp-Max and Belsorp-Aqua Porosimeter. Magnetic measurements were carried out at 300 K using a vibrating sample magnetometer (Microsense EV9). TEM images were recorded on a Philips Tecnai G^2 30 transmission electron microscope with 300 kV accelerating voltage. SEM and EDX analysis was performed using a Hitachi S-3700 M microscope. PL measurements were carried out using Horiba Jobin Yvon equipment employing a CW xenon lamp source at room temperature. TL glow curves of the compacted (Er, F) co-doped SnO_2 samples were recorded using a Harshaw HT Reader 3500 at a heating rate of 3 K/s. Kinetic parameters were determined by the glow curve deconvolution method as implemented in the Glow Fit V1.1 program developed and distributed by Puchalska and Bilski [24]. XPS measurements were carried out using a Thermo K_α XPS instrument at a pressure of better than 10^{-9} Torr. The core-level spectra were collected using MgK_α radiation (photon energy = 1253.6 eV) at a pass energy of 50 eV, an electron take-off angle of 90°, and a resolution of 0.1 eV.

3. Results and discussion

The PXRD pattern of 1 mol% Er-doped $KSnF_3$ (Figures 1a and 1b) obtained by a simple and green precipitation procedure is shown in Figure 1a, and it showed triclinic symmetry as reported in JCPDS file no. 81-1104. No other crystalline impurity was observed in the pattern. The PXRD pattern of the oxidation product of Er-doped $KSnF_3$ with H_2O_2 suggested the formation of rutile-structured SnO_2 (JCPDS file no. 41-1445) (Figure 1a). The average crystallite size estimated from the Scherrer analysis is ∼3 nm. The elemental mapping by EDX analysis of the SEM image of this sample is shown in the inset of Figure 1a, indicating the presence of Er and F in addition to Sn and O in the samples. For the purpose of comparison, 1 mol% Er-doped SnO_2 was synthesized by reacting a mixture of $SnCl_2.2H_2O$ and $ErCl_3$ with H_2O_2 in methanol. Its PXRD pattern is presented in Figure 1a.

To quantify the elements in the co-doped SnO_2 sample, high-resolution core-level XPS spectral analysis was performed and is reproduced in Figure 2. The binding energies were calibrated using the C 1s hydrocarbon peak at 284.6 eV to compensate for surface charging effects. Peaks observed at 487.09 eV, 531.43 eV, and 684.94 eV were assigned to Sn $3d_{5/2}$, O1s, and F1s, respectively, based on earlier reports [17,25]. Deconvolution of the F1s peak suggested the presence of 2 different types of fluoride, i.e. surface and substituted. The peak present at a lower binding energy (684.47 eV) was attributed to the fluoride on the surfaces and the other peak present at a higher binding energy (685.78 eV) was assigned to fluoride ions substituted in the lattice [26]. Furthermore,

the Gaussian fit of Sn $3d_{5/2}$ showed the peaks positioned at 486.98 eV and 488.07 eV arising primarily from Sn^{4+} species. No contribution from elemental Sn^0 atoms and Sn^{2+} ions was noticed, usually known to occur at a binding energy of 485–486 eV [27]. The O1s peak, on deconvolution, gave 2 different types of oxygen. The peak at around 531.39 eV was assigned to O-Sn^{4+} bonding and the peak at 531.87 eV was attributed to the nonstoichiometric oxides present in the surface region [28,29]. The atomic concentrations of Sn, O, and F were 23%, 44%, and 33%. The peak due to Er was not noticed in XPS due to its very low concentration, thus limiting its detection beyond a specific depth.

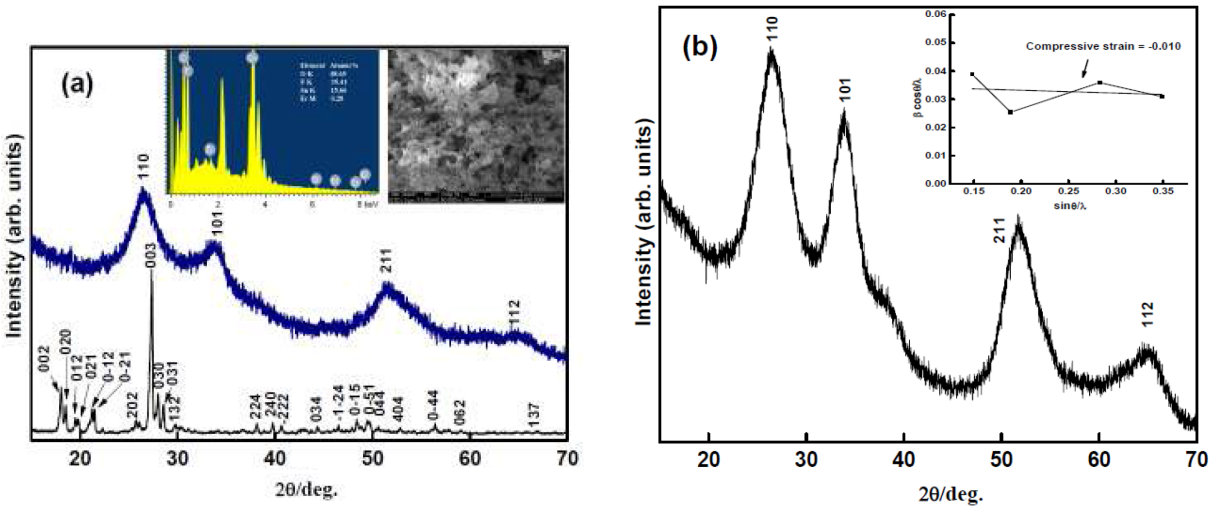

Figure 1. a) PXRD pattern of 1 mol% Er-doped $KSnF_3$ (black line) and oxidized product from 1 mol% Er-doped $KSnF_3$ (blue line). Inset shows SEM image and EDX analysis of the oxidized product from 1 mol% Er-doped $KSnF_3$. b) PXRD pattern of 1 mol% Er-doped SnO_2. Inset shows Williamson–Hall plot of Er-doped SnO_2.

Generally, a major contribution to the broadening of the Bragg reflections was obtained from the strain present in the crystallites as well as their reduced size. The strain in the co-doped sample was calculated following the Williamson and Hall theorem [30]:

$$\beta \cos\frac{\theta}{\lambda} = \frac{1}{D} + \eta \sin\frac{\theta}{\lambda}$$

where β is the full width at half-maximum in radian, $\theta$is the diffraction angle, $\lambda$is the X-ray wavelength, $D$is the effective particle size, and $\eta$is the effective strain. The strain and the crystallite size (D) were measured from the slope and from the intercept of linear fit of $\beta\cos\theta/\lambda$versus $\sin\theta/\lambda$, respectively. A positive slope of +0.020 indicated the tensile strain across (Er, F) co-doped SnO_2 nanocrystals arising from the reduced size of the crystallites (Figure 3) [31]. Since the doped fluoride ion concentration was quite high (with the simultaneous presence of lower valent Er^{3+}), to maintain charge balance, increase in density of oxygen vacancies (OVs) might occur. As a result, the effective columbic repulsion between the tin ions would also increase, contributing to the strain of these crystals. The Williamson and Hall plot of Er-doped SnO_2 (shown in the inset of Figure 1b) suggested a positive compressive strain in the samples, making clear that co-doping was indeed responsible for the tensile strain in these samples. Though these results gave only qualitative information, the effect of them can be realized from the peak shapes in Raman and PL spectra, as discussed later. The calculated crystallite size from the intercept was ~4 nm for (Er, F) co-doped SnO_2 nanocrystals, matching well with the average crystallite size estimated using Scherrer analysis.

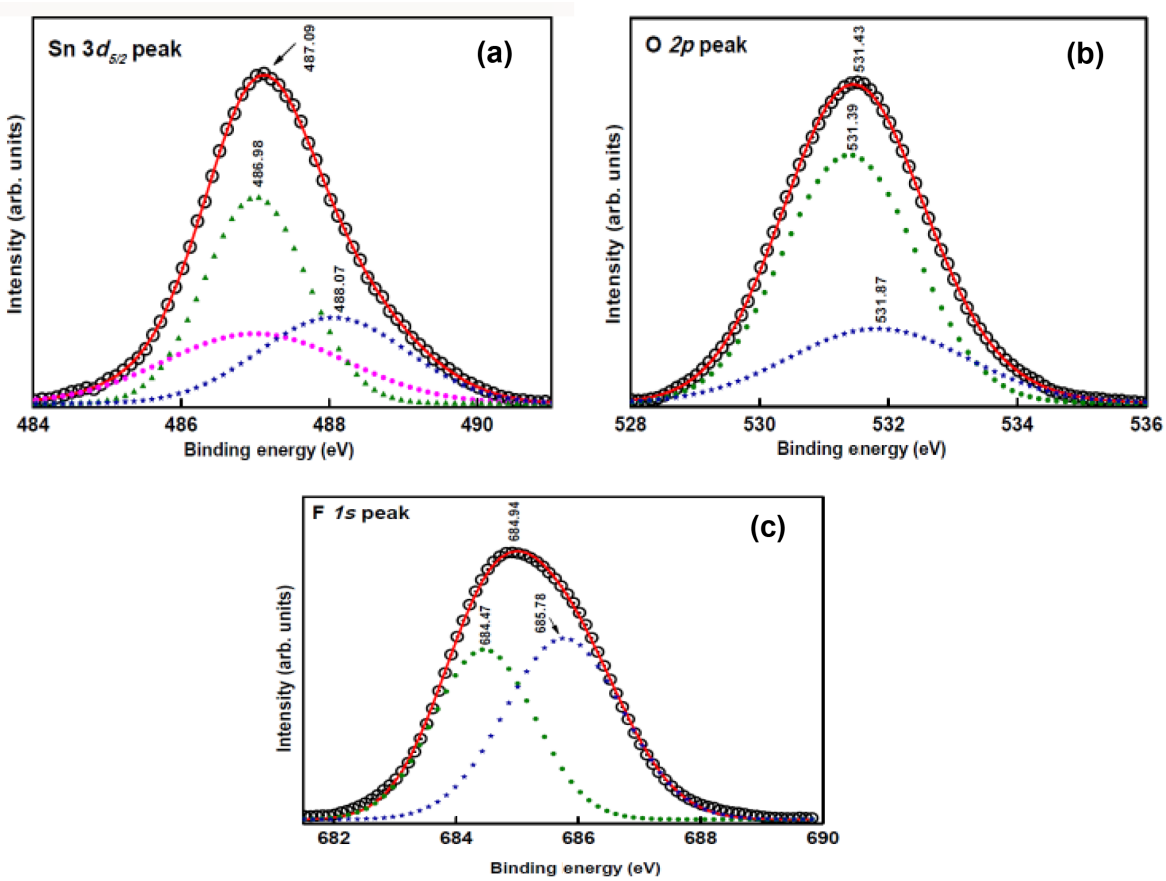

Figure 2. XPS core level spectra of (Er, F) co-doped SnO_2 of Sn*3d*$_{5/2}$, O*2p*, and F*1s*.

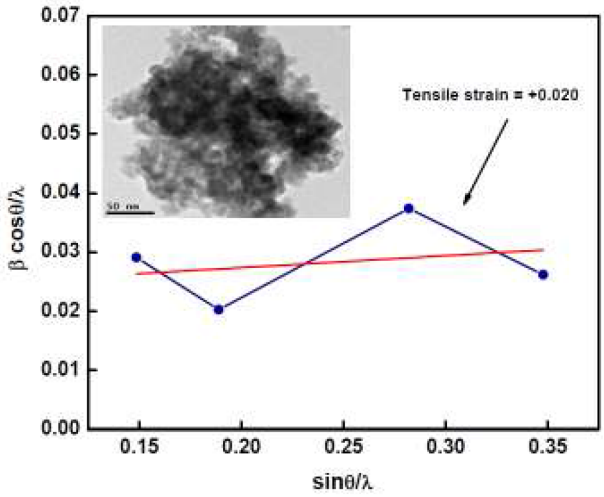

Figure 3. Williamson-Hall plot of (Er, F) co-doped SnO_2. Inset shows TEM image of (Er, F) co-doped SnO_2.

Agglomeration of particles, due to high surface forces such as van der Waals and capillary forces, was observed in the TEM images (shown in the inset of Figure 3). The crystallite size, from TEM images, was in agreement with the Scherrer analysis. A porous morphology was revealed in the SEM micrographs of (Er, F) co-doped SnO_2 (inset of Figure 1a), which was further confirmed from BET analysis. N_2 adsorption–desorption

isotherms of (Er, F) co-doped SnO_2 and Er-doped SnO_2 (Figure 4a). The corresponding pore properties, including BET surface area, pore volumes, and pore sizes, are summarized in Table 1. Mean pore diameter increased from 2.62 nm (Er-doped SnO_2) to 25.82 nm ((Er, F) co-doped SnO_2) and indicated change in the porosity of the sample arising primarily from the heavy anion (F^-) doping of the system. Although such values were reported earlier [32,33], the observed mesopore size was higher than in the singly doped SnO_2 systems. (Er, F) co-doped SnO_2 at room temperature exhibited characteristic curve-type IV isotherms with distinct capillary condensation steps, suggesting uniform mesopores [32,33]. Thermogravimetric traces of (Er, F) co-doped and Er-doped SnO_2 samples in flowing nitrogen atmosphere are presented in Figure 4b. While (Er, F) co-doped SnO_2 showed a slow and gradual weight loss up to 17% in the temperature range of 50–900 °C, drastic weight loss was observed for the Er-doped SnO_2. From the gradual weight loss behavior, it was clear that the dopants in SnO_2 were homogeneously distributed and were thermally stable in the temperature range investigated.

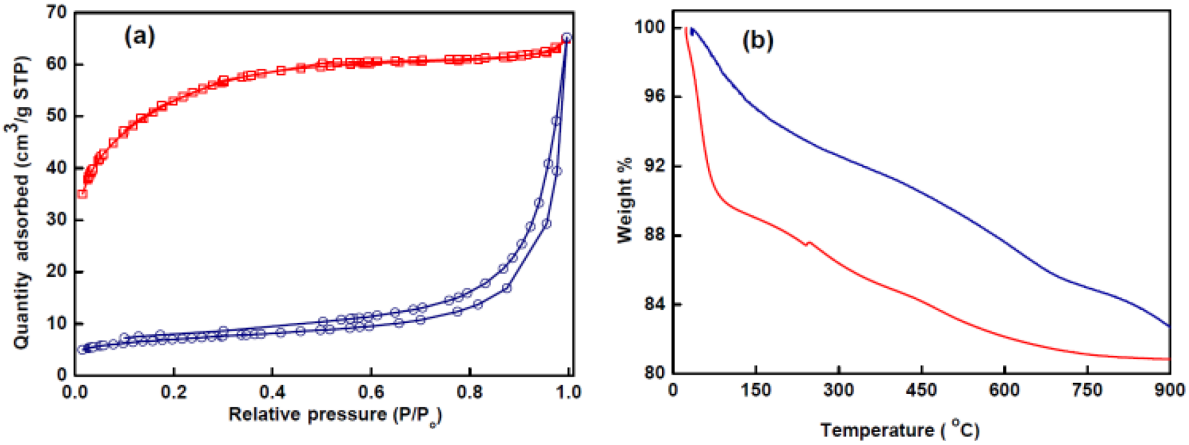

Figure 4. a) Adsorption–desorption isotherm of (Er, F) co-doped SnO_2 (blue circle) and Er-doped SnO_2 (red square). b) Thermogravimetric analysis of (Er, F) co-doped SnO_2 (blue line) and Er-doped SnO_2 (red line).

Table 1. BET surface area, mean pore diameter, and total pore volume of (Er, F) co-doped SnO_2 and Er-doped SnO_2.

Compound	BET surface area (m^2/g)	Mean pore diameter (nm)	Total pore volume (cm^3/g)
(Er, F) co-doped SnO_2	23.42	25.82	0.1009
Er-doped SnO_2	175.21	2.62	0.1002

The FT-IR spectrum of (Er, F) co-doped SnO_2 nanocrystals is shown in the inset of Figure 5a, in which bands at 562 cm^{-1} and 640 cm^{-1} corresponding to the Sn-O vibrations can be located. The weakened intensity of the vibrational band at 640 cm^{-1} was attributed to the inclusion of higher amounts of fluoride in the SnO_2 lattice [17]. The blue shift of the band centered at 562 cm^{-1} (for the co-doped sample) from 553 cm^{-1} (for the heavily F-doped SnO_2 sample) suggested the presence of higher concentration of OVs in them. The Raman spectrum of the (Er, F) co-doped SnO_2 nanocrystals is shown in Figure 5a. For comparison, the Raman spectrum of Er-doped SnO_2 is also presented in Figure 5a. Vibrational modes at 510, 588, 985, 1065, 1220, and 1353 cm^{-1} were observed for the (Er, F) co-doped SnO_2, while the Er-doped SnO_2 showed bands at 323, 446, 570, 624, and 771 cm^{-1}. The band centered at 588 cm^{-1} for (Er, F) co-doped SnO_2 nanocrystals was broad and intense, arising probably from the presence of higher concentrations of in-plane OVs and the inhomogeneous

strain present in the nanocrystals [34,35]. This peak was deconvoluted into 4 peaks centered at 588 cm^{-1} (R1), 554 cm^{-1} (R2), 462 cm^{-1} (R3), and 635 cm^{-1} (R4) as shown in Figure 5b. Peaks R1 and R2 were related to surface defects and R3 and R4 are fundamental modes E_g and A_{1g} (the bending mode of Sn-O-Sn) of SnO_2, respectively [36]. The band at 446 cm^{-1} for Er-doped SnO_2 and at 462 cm^{-1} for (Er, F) co-doped SnO_2 nanocrystals might arise from deeper OVs [37]. The interaction of Er^{3+}/F^- ions in the SnO_2 lattice created changes in the vibrational modes, which are reflected in the disappeared and/or reduced Raman intensity [38]. Relaxation of the $k = 0$ selection rule occurs in nanocrystals when the rate of disorder increases or the size decreases, and the infrared modes become weakly active when the structural changes induced by disorder and size effects take place [39]. For nanocrystals of SnO_2 (less than 16 nm in size), contributions from multiphonon processes are also observed in the high-frequency zone of the Raman spectrum [40]. The bands observed at 985, 1065, 1220, and 1353 cm^{-1} in Figure 5a might possibly arise from the multiphonon scattering corresponding to (E_g+E_g), (E_g+A_{1g}), $(A_{1g}+A_{1g})$, and $(A_{1g}+B_{2g})$ combinations, respectively. Earlier, such observations were reported for specific morphologies of pure SnO_2 (such as nanowires and nanobelts) [41,42]. Such multiphonon scattering was not present in Er-doped SnO_2 samples (Figure 5a). The presence of multiphonon scattering suggested the existence of deeper and shallow traps in (Er, F) co-doped SnO_2, which were experimentally detected employing TL spectroscopy measurements.

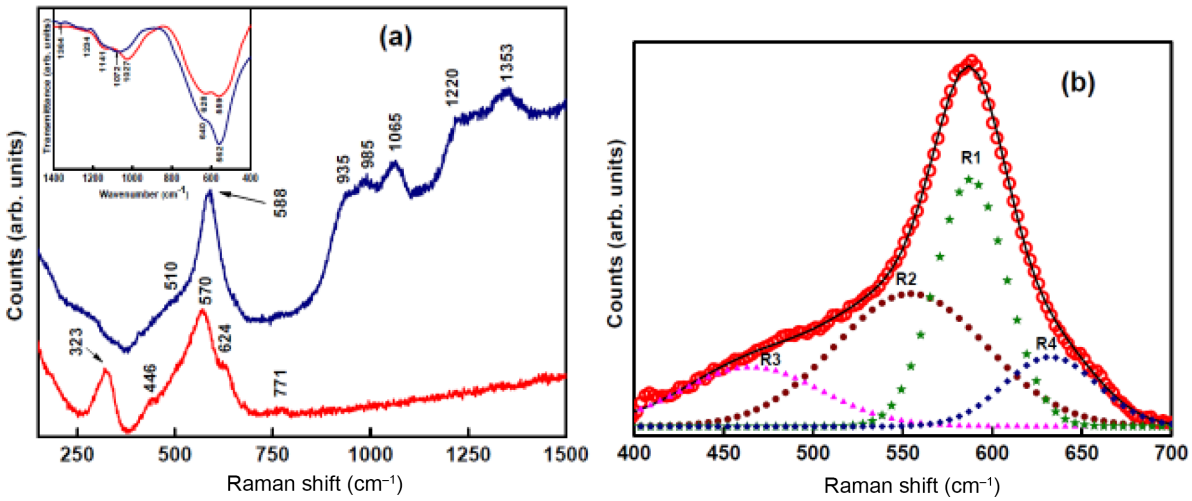

Figure 5. a) Raman spectrum of (Er, F) co-doped SnO_2 (blue line) and Er-doped SnO_2 (red line). Inset shows FT-IR spectrum of (Er, F) co-doped SnO_2 (blue circle) and Er-doped SnO_2 (red square). b) Deconvoluted Raman spectrum of (Er, F) co-doped SnO_2.

Diffuse reflectance spectra are shown in Figures 6a–6c. A large blue shift of the exciton absorption was observed in the UV-Vis diffuse reflectance spectrum of (Er, F) co-doped SnO_2 (Figure 6a) and the estimated band gap by the Kubelka–Munk function analysis was 4.18 eV (Figure 6c). The shift could be due to the combined effect of quantum size and the Moss–Burstein effects [43,44]. Additional experiments on the variation of absorption edge with temperature can provide crucial information on thermal activation threshold of this co-doped system as its shape is greatly influenced by the carrier–phonon interaction and the carrier–impurity interactions with increasing temperature. The UV-Vis diffuse reflectance spectrum of Er-doped SnO_2 is presented in Figure 6b. The inclusion of Er^{3+} in SnO_2 was confirmed from the presence of sharp bands

arising from intraconfigurational $f-f$ transitions from the $^4I_{15/2}$ ground state to the $^4I_{11/2}$, $^4I_{9/2}$, $^4F_{9/2}$, $^2H_{11/2}$, $^4F_{7/2}$, and $^4F_{5/2}$ excited states [16] (shown in the inset of Figure 6b). In addition to the $f-f$ transitions, a red shift of the band gap with respect to (Er, F) co-doped SnO_2 sample was noticed (Figure 6c). The red shift might be from fewer OVs in singly Er^{3+}-doped SnO_2 as compared to (Er, F) co-doped SnO_2.

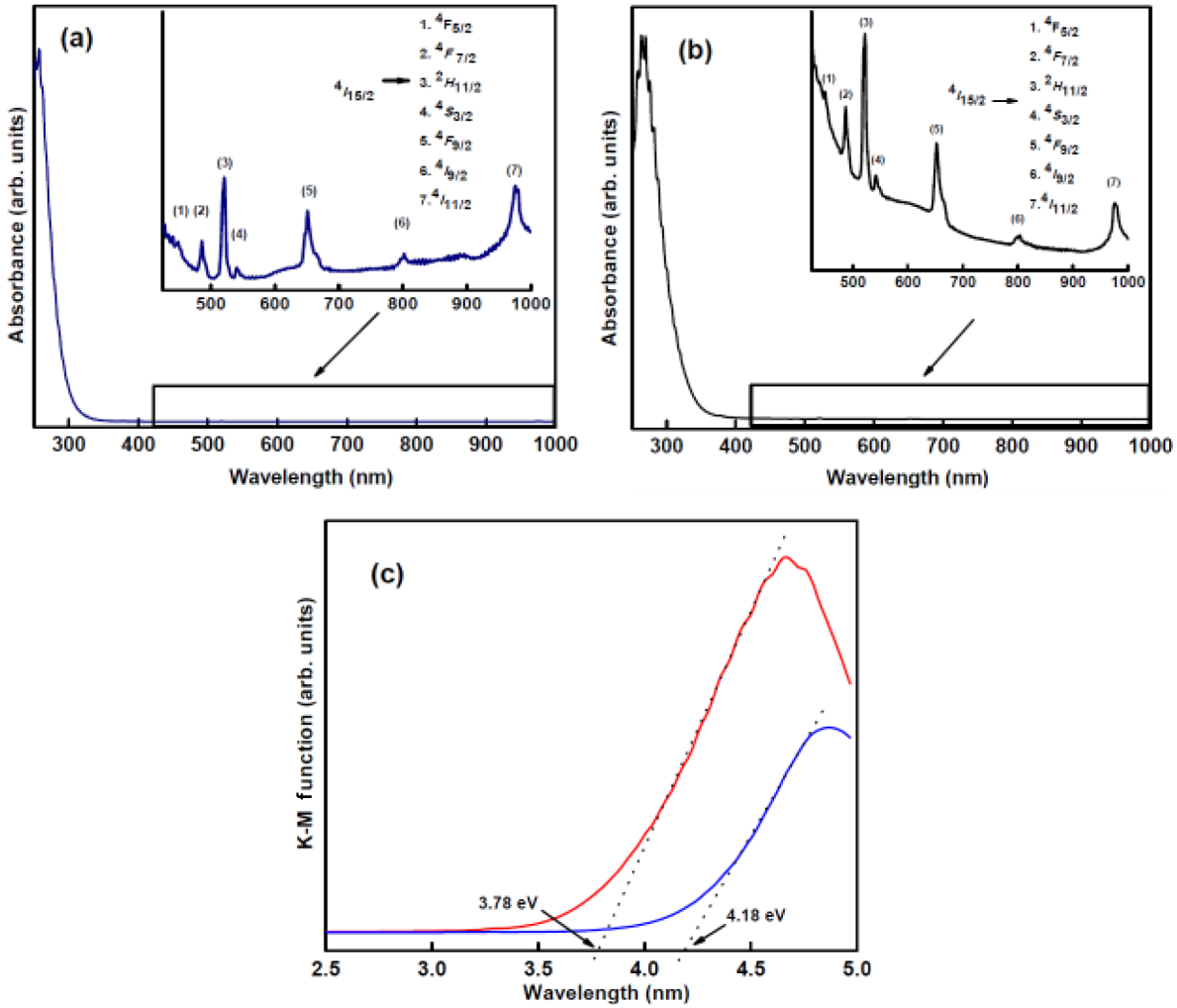

Figure 6. a) Diffuse reflectance spectra of (Er, F) co-doped SnO_2, Inset shows expanded portion from 425 nm to 1000 nm. b) Diffuse reflectance spectrum of Er-doped SnO_2. Inset shows the expanded portion from 425 nm to 1000 nm. c) Plot of absorbance versus photon energy of (Er, F) co-doped SnO_2 (blue line) and Er-doped SnO_2 (red line).

The PL spectrum of (Er, F) co-doped SnO_2 in comparison to the Er-doped SnO_2 sample at room temperature is shown in Figure 7a. Increased intensity of the PL emission from (Er, F) co-doped SnO_2 samples was quite evident. The broad PL emission centered at 540 nm might be from defect electronic states as a result of co-doping as well as due to the inhomogeneous strain present in these nanocrystals. Such defect states might also be possible by 'bridging' OVs. In such a situation, electron excitation to the bulk shallow energy levels followed by return to the intragap level of SnO_2 corresponding to oxygen surface vacancies via radiative transitions might occur [45]. Presence of shoulder bands at 596 nm and 645 nm indicated strong orange and red emission, respectively. This strong orange luminescence was related to the bridging and in-plane OVs, which

form a series of metastable energy levels within the band gap [46]. The presence of broad luminescence bands in the range of 350–750 nm for the co-doped SnO_2 sample at room temperature suggested the existence of shallow trapped states within the band gap consisting of several subbands [47]. Upon deconvolution, 3 subbands at 471 nm, 546 nm, and 627 nm (Figure 7b) were evident, indicating the presence of 3 types of emission centers. The nature of the transition causing these emissions was generally thought to be Sn or O vacancies formed during the doping process, inducing deeper trapping states within the band gap. The band at 471 nm may originate from a shallower energy level located in the band gap compared to that of the 546 nm luminescence, as reported earlier [48]. The green emission at 546 nm and red emission at 627 nm could be from the $f-f$ transitions, ${}^4S_{3/2} \rightarrow {}^4I_{15/2}$ and ${}^4F_{9/2} \rightarrow {}^4I_{15/2}$, of Er^{3+} ions, respectively. From the Raman and PL spectroscopy results, it was clear that the (Er, F) co-doped SnO_2 system was highly disordered in nature, consisting of many OVs.

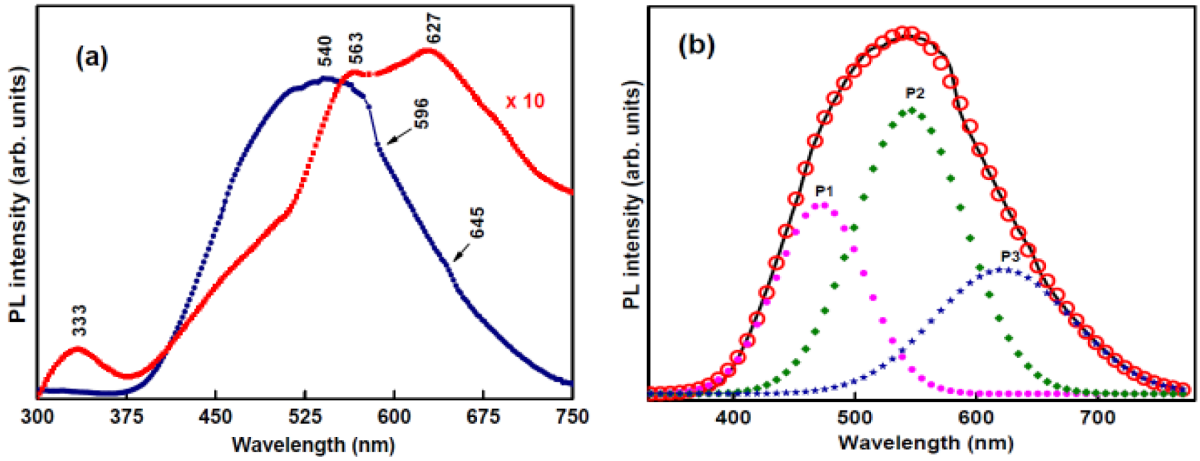

Figure 7. a) PL emission spectra of (Er, F) co-doped SnO_2 (blue circle) and Er-doped SnO_2 (red square). b) Deconvoluted PL spectrum of (Er, F) co-doped SnO_2.

Without external irradiation, the (Er, F) co-doped SnO_2 nanocrystals showed a broad intense glow curve at 485 K and a weak emission at 600 K in the TL spectrum, signifying the presence of trapped states and shallow deeper traps, respectively (Figure 8a). It is noteworthy that no glow peak was observed for the Er-doped SnO_2 in the temperature range of 350–650 K (Figure 8a). Additionally, the glow curve in the (Er, F) co-doped SnO_2 occurred at a slightly higher temperature as compared to the heavily F-doped SnO_2 system (448 K) [18]. The OVs, due to the heavy doping of O^{2-} ions with the F^- ions, and the hole created by the co-dopant Er^{3+} might possibly interact, leading to the formation of an appreciable concentration of trapped states resulting in intense TL emission [49]. In addition to this simple correlation, the (Er, F) co-doping might be creating deeper traps and increasing the density of the existing traps in addition to enhancing TL intensity. The creation of more OVs due to the introduction of F^- and Er^{3+} in the lattice suggested the possibility of creation of F and F^+ centers in the system. The trapped emission also demonstrated the correlation between the emission energy of the surface states and the quantum size effects in this system. The size effects on the surface states in the TL glow curves were discussed in detail in previous reports [50]. There are indications that OVs might be serving as traps for free electrons giving F^+ ($e_O^{\bullet\bullet}$) or F ($V_O^{\times}$) centers while holes are temporarily immobilized in the vicinity of $Er_{Sn}^{\times}$ giving [$Er_{Sn}^{\times}$-$h^{\bullet}$] entities. Alternatively, holes can also be trapped in the Er_{Sn} site due to its net negative charge, giving [Er_{Sn}-$h^{\bullet}$] [51]. The glow curve obtained at a heating rate of 3 K s^{-1} for the (Er, F)

co-doped SnO_2 crystals were deconvoluted into 4 first-order peaks by the Glow Fit computer program (Figure 8b). The heavily F-doped SnO_2 system showed 3 types of traps [18]. The figure of merit (FOM), a parameter describing the quality of fitting, was calculated [24]. The values of kinetic parameters of the glow curve of (Er, F) co-doped SnO_2 at a heating rate of 3 K s^{-1} were calculated by GCD method, Chen's formulae, Grossweiner analysis, and Kivits Hagebeuk analysis and are presented in Table 2 [52–54]. The variation in TL intensities for (Er, F) co-doped SnO_2 nanocrystals on exposure to UV light (using a 125-W high vapor pressure mercury lamp) for 5, 10, and 15 min at a linear heating rate of 3 K s^{-1} are shown in the inset of Figure 8a. The intensity of the glow peaks decreased and shifted towards higher temperatures with UV irradiation time. This effect is sometimes referred to as 'radiation damage' in the literature [55]. This type of behavior is quite opposite to that of the heavily F-doped SnO_2 system, where the intensity of the glow curves increased on exposure to UV irradiation.

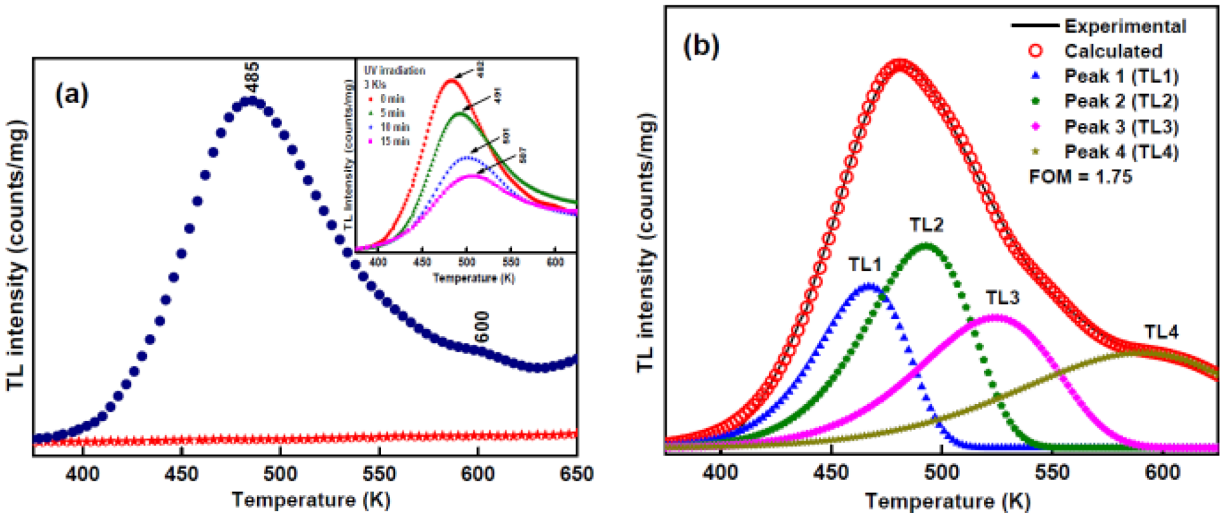

Figure 8. a) TL glow curve of (Er, F) co-doped SnO_2 (blue circles) and Er-doped SnO_2 (red stars). Inset shows TL glow curves of (Er, F) co-doped SnO_2 recorded at 3 K s^{-1} after irradiating it with UV light for 0, 5, 10, and 15 min. b) Glow-fitting curve (black solid line) and deconvoluted peaks of (Er, F) co-doped SnO_2 obtained by the Glow Fit program on the experimental TL curve (red circles).

Table 2. Summary of the trap depth (E) values, frequency factor (S), and FOM of glow curve 1 of the (Er, F) co-doped SnO_2 fitted by various methods.

TL deconvoluted peak	T_m (K)	Trap depth (eV)				S (s^{-1}) (GCD)	FOM %
		Glow curve shape methods			Glow fit		
		Chen [52]	Grossweiner et al. [53]	Kivitis and Hagebeuk [54]			
TL1	467	0.89	0.94	0.87	0.89	5.66E+08	1.76
TL2	493	0.84	0.90	0.84	0.85	5.65E+07	
TL3	524	0.71	0.77	0.71	0.72	8.16E+05	
TL4	591	0.55	0.60	0.55	0.55	2.44E+03	

The room-temperature ferromagnetism observed in nanosized ZnO, SnO_2, and TiO_2, which are otherwise diamagnetic, has created immense interest in understanding the interactions between the surface OVs

existing in these systems [7,23]. The room-temperature magnetization of (Er, F) co-doped SnO_2 showed significant hysteresis at room temperature, possibly from a ferromagnetic ordering, as presented in Figure 9. The coercivity was found to be ∼180 Oe at room temperature. Ferromagnetism might be missing from the exchange interactions between the unpaired electron spins arising from defects and OVs at the surface of the nanocrystals. It has been suggested that room-temperature ferromagnetism results from the magnetic coupling between $V_o^{\bullet}$ centers at the surface of the nanoparticles [23,56,57]. The ferromagnetic behavior of Er-doped SnO_2 is slightly different from that of (Er, F) co-doped SnO_2. After showing a small hysteresis in low fields, the magnetization of (Er, F) co-doped SnO_2 increased linearly in higher fields. This type of linear behavior might be attributed to the magnetic moment associated with the conduction electrons [58].

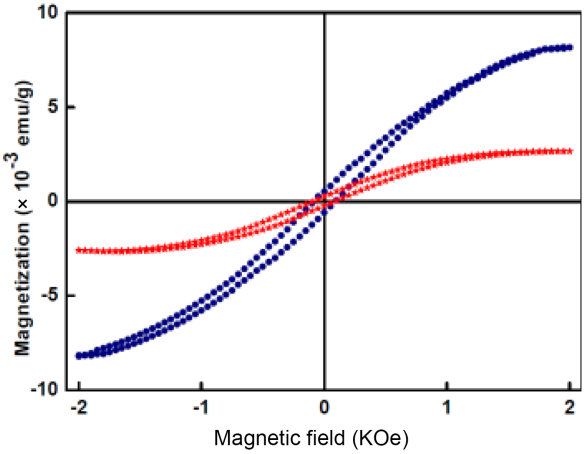

Figure 9. Plot of magnetization versus magnetic field of (Er, F) co-doped SnO_2 (blue circle) and Er-doped SnO_2 (red stars).

4. Conclusion

The interaction of the hole created by the doping of an f-block element with the vacancies generated due to heavy doping of fluoride in SnO_2 nanocrystals has been studied for the first time. Widening of the band gap due to the combined effect of quantum confinement and Moss–Burstein effect occurred with the co-doping of SnO_2, yielding a value of 4.18 eV. The presence of huge OVs that are highly disordered is observed in co-doped samples. The presence of multiphonon interactions, which were earlier reported only in SnO_2 nanostructures such as nanowires and nanorods, are observed in the Raman and IR spectra of (Er, F) co-doped SnO_2 nanocrystals exhibiting spherical morphology. Pore size analysis revealed significant porosity in co-doped samples with mean pore diameter of 25.82 nm. The samples also showed increased thermal stability over a wide range of temperature (50–900 °C). Strong green luminescence observed in PL of (Er, F) co-doped SnO_2 nanocrystals suggests their potential use in optoelectronic devices such as LEDs. Additionally, the co-doped samples without any external irradiation exhibited glow curves in the TL spectra, signifying the presence of deeper traps in the system. Irradiating the co-doped samples with UV light for different intervals of time resulted in the resolution of the glow curves. (Er, F) co-doped SnO_2 nanocrystals are quite environmentally friendly, robust, and relatively simple to fabricate in different sizes in larger quantities and therefore can be used as active temperature and UV light sensors in places where direct contact sensors fail. The co-doping approach has stabilized ferromagnetism at room temperature.

Acknowledgments

This work was financially supported by the DST (SR/S1/PC-07/2011), Government of India, and the University of Delhi under the "Scheme to Strengthen R&D Doctoral Research Program". The timely help of Dr P Senthil Kumar, Department of Physics and Astrophysics, University of Delhi, in XPS measurements is gratefully acknowledged. One of the authors, Vinod Kumar, thanks the CSIR, New Delhi, for SRF.

References

[1] Gordon, R. G. *MRS Bull.* **2000**, 52–57.

[2] Nagarajan, R.; Kumar, V.; Ahmad, S. *Indian J. Chem.* **2012,** *51A*, 145–154.

[3] Kumar, N.; Maitra, U.; Hegde, V. I.; Waghmare, U. V.; Sundaresan, A.; Rao, C. N. R. *Inorg. Chem.* **2013**, *52*, 10512–10519.

[4] Kim, Y. I.; Seshadri, R. *Inorg. Chem.* **2008**, *47*, 8437–8443.

[5] Hegde, M. S.; Madras, G.; Patil, K. C. *Acc. Chem. Res.* **2009**, *42*, 704–712.

[6] Okabayashi, J.; Nomura, K.; Kono, S.; Yamada, Y. *Jpn. J. Appl. Phys.* **2012**, *51*, 023003.

[7] Nomura, K.; Okabayashi, J.; Okamura, K.; Yamada, Y. *J. Appl. Phys.* **2011**, *110*, 083901.

[8] Govindan, K.; Murugasen, S.; Maruthamuthu, P. *Mater. Res. Bull.* **2013**, *48*, 1913–1919.

[9] Kang, Q.; Yuan, B.; Xu, J.; Fu, M. L. *Catal. Lett.* **2011,** *141*, 1371–1377.

[10] Tagliente, M. A.; Bello, V.; Pellegrini, G.; Mattei, G.; Mazzoldi, P.; Massaro, M. *J. Appl. Phys.* **2009**, *106*, 104304.

[11] Batzill, M.; Diebold, U. *Prog. Surf. Sci.* **2005**, *79*, 47–154.

[12] Turgut, G.; Keskenler, E. F.; Aydın, S.; Yılmaz, M.; Doğan, S.; Düzgün, B. *Phys. Scr.* **2013**, *87*, 035602.

[13] Huang, J.; Pei, X.; Ji, F. *Adv. Mater. Res.* **2012**, *538–541*, 37–43.

[14] Moharrami, F.; Bagheri-Mohagheghi, M. M.; Azimi-Juybari, H. *Thin Solid Films* **2012**, *520*, 6503–6509.

[15] Ghosh, S.; Mandal, M.; Mandal, K. *J. Magn. Magn. Mater.* **2011**, *323*, 1083–1087.

[16] Bouzidi, C.; Moadhen, A.; Elhouichet, H. *Appl. Phys. B* **2008**, *90*, 465–469.

[17] Kumar, V.; Govind, A.; Nagarajan, R. *Inorg Chem.* **2011**, *50*, 5637–5645.

[18] Kumar, V.; Nagarajan, R. *Chem. Phys. Lett.* **2012**, *530*, 98–101.

[19] Bouzigues C.; Gacoin T.; Alexandrou, A. *ACS Nano* **2011**, *5*, 8488–8505.

[20] Morais, E. A.; Scalvi, L. V. A. *J. Eur. Ceram. Soc.* **2007**, *27*, 3803–3806.

[21] Castillo, J. D.; Rodríguez, V. D.; Yanes, A. C.; Méndez-Ramos, J. *J. Nanopart. Res.* **2008**, *10*, 499–506.

[22] Kataoka, T.; Yamazaki, Y.; Singh, V. R.; Sakamoto, Y.; Fujimori, A.; Takeda, Y.; Ohkochi, T.; Fujimori, S. I.; Okane, T.; Saitoh, Y. et al. *Appl. Phys. Lett.* **2011**, *99*, 132508.

[23] Sundaresan, A.; Bhargavi, R.; Rangarajan, N.; Siddesh, U.; Rao, C. N. R. *Phys. Rev. B* **2006**, *74*, 161306.

[24] Puchalska, M.; Bilski, P. *Radiat. Meas.* **2006**, *41*, 659–664.

[25] Scofield, J. H. *J. Electron. Spectrosc.* **1976**, *8*, 129–137.

[26] Martinez, A. I.; Huerta, L.; Rueda De Leon, J. M. O.; Acosta, D.; Malik, O.; Aguilar, M. *J. Phys. D* **2006**, *39*, 5091–5096.

[27] Zhou, Z. B.; Cui, R. Q.; Hadi, G. M.; Li, W. Y.; Ding, Z. M. *J. Mater. Sci. Mater. Electron.* **2001**, *12*, 417–421.

[28] Kwoka, M.; Ottaviano, L.; Passacantando, M.; Santucci, S.; Czempik, G.; Szuber, J. *Thin Solid Films* **2005**, *490*, 36–42.

[29] Wang, C.; Du, G.; Ståhl, K.; Huang, H.; Zhong, Y.; Jiang, J. Z. *J. Phys. Chem. C* **2012**, *116*, 4000–4011.

[30] Williamson, G. K.; Hall, W. H. *Acta Metall.* **1953**, *1*, 22–31.

[31] Xu, X.; Zhuang, J.; Wang, X. *J. Am. Chem. Soc.* **2008**, *130*, 12527–12535.

[32] Qiao, Z.; Brown, S. S.; Adcock, J.; Veith, G. M.; Bauer, J. C.; Payzant, E. A.; Unocic, R. R.; Dai, S. *Angew. Chem. Int. Ed.* **2012**, *51*, 2888–2893.

[33] Shin, J.; Choi, S. J.; Lee, I.; Youn, D. Y.; Park, C. O.; Lee, J. H.; Tuller, H. L.; Kim, I. D. *Adv. Funct. Mater.* **2013**, *23*, 2357–2367.

[34] Merle, P.; Pascual, J.; Camassel, J.; Mathieu, H. *Phys. Rev. B* **1980**, *21*, 1617–1626.

[35] Liu, Z, L.; Wu, X. L.; Gao, J. C.; Shen, T.; Li, H.; Chu, P. K. *Solid State Commun.* **2011**, *151*, 811–814.

[36] Tran, T. V.; Turrell, S.; Eddafi, M.; Capoen, B.; Bouazaoui, M.; Roussel, P.; Berneschi, S.; Righini, G.; Ferrari, M.; Bhaktha, S. N. B. et al. *J. Molecular Struct.* **2010**, *976*, 314–319.

[37] Liu, L. Z.; Li, T. H.; Wu, X. L.; Shen, J. C.; Chu, P. K. *J. Raman Spectrosc.* **2012**, *43*, 1423–1426.

[38] Pillai, S. K.; Sikhwivhilu, L. M.; Thembela K. H. *Mater. Chem. Phys.* **2010**, *120*, 619–624.

[39] Campbell, I. H.; Fauchet, P. M. *Solid State Commun.* **1986**, *58*, 739–741.

[40] Diéguez, A.; Romano-Rodríguez, A.; Vilà, A.; Morante, J. R. *J. Appl. Phys.* **2001**, *90*, 1550–1557.

[41] Mahan, G. D.; Gupta, R.; Xiong, Q.; Adu, C. K.; Eklund, P. C. *Phys. Rev. B* **2003**, *68*, 073402.

[42] Riera, R.; Rosas, R.; Marin, J. L.; Bergues, J. M.; Campoy, G. *J. Phys. Condens. Matter* **2003**, *15*, 3225–3248.

[43] Brus, L. E. *IEEE J. Quantum Electron.* **1986**, *22*, 1909–1914.

[44] Abram, A.; Rees, G. J.; Wilson, B. L. H. *Adv. Phys.* **1978**, *27*, 799–892.

[45] Luo, S. H.; Chu, P. K.; Liu, W. L.; Zhang, M.; Liu, C. L. *Appl. Phys. Lett.* **2006**, *88*, 183112.

[46] Cox, D. F.; Fryberger, T. B.; Semancik, S. *Phys. Rev. B* **1988**, *38*, 2072–2083.

[47] Hu, J. Q.; Bando, Y.; Liu, Q. L.; Golberg, D. *Adv. Funct. Mater.* **2003**, *13*, 493–496.

[48] Luo, S.; Jiyang Fan, J.; Liu, W.; Zhang, M.; Song, Z.; Lin, C.; Wu, X.; Chu, P. K. *Nanotechnology* **2006**, *17*, 1695–1699.

[49] Ambrico, P. F.; Ambrico, M.; Colaianni, A.; Schiavulli, L.; Dilecce, G.; De Benedictis, S. *J. Phys. D* **2010**, *43*, 325201.

[50] Chen, W.; Wang, Z.; Lin, Z.; Lin, L. *Appl. Phys. Lett.* **1997**, *70*, 1465–1467.

[51] Trojan-Piegza, J.; Niittykoski, J.; Hölsä J.; Zych, E. *Chem. Mater.* **2008**, *20*, 2252–2261.

[52] Chen, R. *J. Electrochem. Soc.* **1969**, *116*, 1254–1257.

[53] Grossweiner, L. I. *J. Appl. Phys.* **1953**, *24*, 1306–1307.

[54] Kivits, P.; Hagebeuk, H. J. L. *J. Lumin.* **1977**, *15*, 1–27.

[55] Lawless, J. L.; Chen, R.; Lo, D.; Pagonis, V. *J. Phys. Condens. Matter* **2005**, *17*, 737–753.

[56] Dutta, D.; Bahadur, D. *J. Mater. Chem.* **2012**, *22*, 24545–24551.

[57] Kaspar, T. C.; Heald, S. M.; Wang, C. M.; Bryan, J. D.; Droubay, T.; Shutthanandan, V.; Thevuthasan, S.; McCready, D. E.; Kellock, A. J.; Gamelin, D. R. et al. *Phys. Rev. Lett.* **2005**, *95*, 217203.

[58] Tahir, N.; Karim, A.; Persson, K. A.; Hussain, S. T.; Cruz, A. G.; Usman, M.; Muhammad, N.; Qiao, R.; Yang, W.; Chuang, Y. D. et al. *J. Phys. Chem. C* **2013**, 117, 8968–8973.